Journal of the European Ceramic Society **17** (1997) 1285–1299

PII: S0955-2219(96)00237-3
0955-2219/97/$17.00

β-Si_3N_4 Grain Growth, Part I: Effect of Metal Oxide Sintering Additives

H. Björklund,[a] L. K. L. Falk,[a]* K. Rundgren[b] and J. Wasén[c]

[a]Department of Physics, Chalmers University of Technology, S-412 96 Göteborg, Sweden
[b]Swedish Ceramic Institute, Box 5403, S-402 29 Göteborg, Sweden
[c]Department of Engineering Metals, Chalmers University of Technology, S-412 96 Göteborg, Sweden

(Received 16 August 1996; revised version received 7 November 1996; accepted 11 November, 1996)

Abstract

Si_3N_4 ceramics with a constant molar fraction of Al_2O_3 and Y_2O_3 or Yb_2O_3 have been microstructurally characterised by scanning electron microscopy in combination with quantitative microscopy, and the three-dimensional β-Si_3N_4 grain size distributions were subsequently reconstructed by a stereological method. The Si_3N_4 ceramics were densified by gas pressure sintering at 1900°C under a pressure of 980 kPa for 1, 3, 5 and 10 h. The microstructural analysis showed that the Y_2O_3/Al_2O_3 ratio in the starting powder mixture affects the β-Si_3N_4 grain shape and size distribution. An increased Y_2O_3/Al_2O_3 ratio resulted in a higher mean aspect ratio. A replacement of Y_2O_3 by Yb_2O_3 increased the mean aspect ratio further and resulted in a more narrow grain size distribution with an increased mean grain volume. The mean grain size increased with densification time, and a grain growth exponent of n = 3·2 implied that the β-Si_3N_4 grain growth was rate controlled by diffusion through the liquid phase. The metal oxide composition also determined the formation of secondary crystalline phases. Crack propagation and, hence, fracture toughness was dependent upon β-Si_3N_4 grain morphology and the intergranular structure.

1 Introduction

It has been shown that the choice of metal oxide and nitride sintering additives has a crucial influence upon grain size and shape of Si_3N_4 ceramics.[1–4] Additions of Y_2O_3 and rare earth metal oxides promote growth of high aspect ratio β-Si_3N_4 grains that act as toughening agent in the self-reinforced Si_3N_4 ceramic.[3–5] Densification of these materials generally requires a comparatively high fraction of sintering additives which results in a larger intergranular volume containing secondary crystalline and/or amorphous phases that may have a negative effect on mechanical and chemical properties. However, balanced starting powder compositions containing also Al_2O_3 and AlN enable the fabrication of duplex α/β sialons.[6,7] The dispersion of elongated β sialon (β') grains in an α sialon (α') matrix results in a sialon ceramic with a favourable combination of toughness and hardness. These microstructures may also be designed to contain only a minimum volume fraction of intergranular residual glass. Al_2O_3 alone results, on the other hand, often in a microstructure consisting of smaller and equiaxed β' grains and, consequently, also in a lower toughness.[3]

The metal oxide and nitride additives react with the surface silica present on the Si_3N_4 starting powder particles and some of the Si_3N_4 whereby an oxynitride liquid phase sintering medium is formed.[1,8,9] The Si_3N_4 undergoes a solution/reprecipitation process; the α-Si_3N_4 in the starting powder is preferentially dissolved and, depending upon chemistry, α', β' or β-Si_3N_4 will crystallise from the liquid. The Si_3N_4 grain morphology will be dependent upon the overall chemistry and the densification temperature.

A fibrous Si_3N_4 microstructure is of advantage in many applications because it gives the ceramic a high toughness through mechanisms such as crack deflection, crack bridging and grain pull-out.[10,11] It is, therefore, of interest to establish relationships between fabricating conditions and β or β' Si_3N_4 grain morphology. There is, however, no analytical solution for relating the apparent grain size and shape which can be imaged on a section through the microstructure to the true three-dimensional (3D) grain size distribution.[12–15]

*To whom correspondence should be addressed.

A stereological method has lately been successfully applied for the determination of the average grain shape (length/width ratio) and the reconstruction of the 3D grain size distribution in β-Si_3N_4 microstructures.[12] The β-Si_3N_4 grain shape was approximated by the hexagonal prism and it was assumed that the grain shape was independent of grain volume. Two-dimensional (2D) and 3D stereological parameters for hexagonal prisms with different aspect ratios were obtained by computer simulations. These data enabled the reconstruction of the 3D grain size distribution from measurements of 2D stereologic parameters on a section through the microstructure.

This paper will focus upon relationships between metal oxide additives, time at densification temperature, β-Si_3N_4 grain morphology and indentation fracture toughness. The Si_3N_4 ceramics were fabricated with a constant molar fraction of the metal oxide additives Al_2O_3 and Y_2O_3 or Yb_2O_3, but with varying cation ratios. The β-Si_3N_4 grain shape and size distributions were determined by quantitative microscopy in combination with the above-mentioned stereological method.

2 Experimental Procedures

2.1 Experimental materials

The Si_3N_4 powder (E-10 grade, Ube Industries Ltd, Japan) was mixed with different amounts of Y_2O_3 (Y-F grade, Mitsubishi Kasei Co., Japan), Al_2O_3 (AKP-30 grade, Sumitomo Electric, Japan) and Yb_2O_3 (High Purity Chemicals, Japan), see Table 1. The Si_3N_4 starting powder has an oxygen content which corresponds to 5·6 mol% SiO_2. The molar fraction of metal oxide additives was 9·5 mol% in all starting powder compositions. Compositions with only Y_2O_3 or Al_2O_3 as well as three compositions with different Y_2O_3/Al_2O_3 molar ratios were prepared. The Y_2O_3/Al_2O_3 ratio in one of the compositions, composition A in Table 1, corresponds to that of the Y,Al-garnet (YAG), $5Al_2O_3{\cdot}3Y_2O_3$. The Y_2O_3 addition in one of the Y_2O_3 and Al_2O_3 compositions was replaced by Yb_2O_3, see Table 1.

The powder mixtures were ball milled in ethanol for 24 h using Si_3N_4 as the milling medium. The slurries were wet-sieved through a 32 μm sieve before vacuum drying at 60°C. The dried powders were sieve granulated through a 250 μm sieve before forming by uniaxial pressing at 20 MPa and cold isostatic pressing at 300 MPa. Densification was performed by gas pressure sintering (GPS) in a graphite resistance heated furnace (Fujidempa Kogyo High Multi 10000) with the specimens placed in a powder bed (50% BN and 50% Si_3N_4) in a Si_3N_4 crucible. The specimens were heated under vacuum up to 1400°C at a rate of 10°C/min. The heating rate between 1400°C and the final densification temperature of 1900°C was 5°C/min. A nitrogen pressure of 200 kPa was applied at 1400°C. The pressure was increased to the final densification pressure of 980 kPa at 1800°C. The specimens were held at 1900°C for 1, 3, 5 and 10 h and were left to cool inside the furnace when it was turned off. The materials are denoted by a letter indicating starting powder composition and a number indicating time at sintering temperature, see Table 1. Bulk densities of the gas pressure sintered materials were measured by Archimedes' method.

2.2 Microstructural analysis

Microstructural characterisation was carried out by scanning electron microscopy (SEM) using a CamScan S4-80DV scanning electron microscope equipped with a Link eXL energy dispersive (EDX) system for elemental analysis. The microstructures were studied on polished and plasma-etched sections. Plasma etching removes, preferentially, the β-Si_3N_4 grains and leaves the intergranular phases as an elevated network. A thin carbon film was evaporated on to the specimens in order to avoid charging under the electron beam.

The phase compositions of materials A1–A10, B5, E5 and F5 were determined by X-ray diffraction (XRD) of polished sections.

Table 1. Starting powder compositions of the materials

Specimen type and time at 1900°C(h)	*Additive composition (wt%)*			*Additive molar ratio*[a] *Y_2O_3(Yb_2O_3)/Al_2O_3*
	Y_2O_3	*Yb_2O_3*	*Al_2O_3*	
A 1, 3, 5, 10	5·7	—	4·3	0·60[b]
B 1, 3, 5, 10	8·7	—	2·8	1·38
C 1, 3, 5, 10	—	—	7·1	—
D 1, 3, 5, 10	14·4	—	—	—
E 1, 3, 5, 10	—	14·2	2·7	1·38
F 1, 3, 5, 10	13·0	—	0·7	8·5

[a]The total molar fraction of metal oxides is 9·5 mol% in all materials.
[b]Composition corresponds to YAG.

2.3 Quantitative microscopy

The microstructures of specimens A1, A3, A5, B5, E5 and F5 were characterised by quantitative microscopy. Enlarged SEM micrographs (final magnification 12000–18000×) of polished and plasma-etched sections were placed on a digitising tablet and the positions of 400–500 grain section corners were registered for each specimen. Before the measurements the grain boundaries were manually marked which included interpretation of uncertain grain boundaries and identifying grain section corners. These adjustments were small compared to the values of the experimental 2D parameters.

A number of 2D stereological parameters were determined from these measurements. The maximum grain section dimension, D_m, the grain section area, A, the shape parameter $Q = 4\pi A/U^2$, where U is the perimeter, and the number of corners, N_c, were determined for each grain section, see Fig. 1. Mean values of these parameters were calculated for the sections through the different microstructures.

The distributions of the shape parameter (Q) and the number of corners per grain section (N_c) depend only on grain shape. The experimental distributions of these parameters were compared with computer-synthesised Q and N_c distributions for hexagonal prisms with different given aspect ratios. This showed that the experimental distributions could be explained as the result of sectioning a prism with a certain aspect ratio. Comparison of experimental $\bar{Q}$ and $\bar{N}_c$ with values of $\bar{Q}$ and $\bar{N}_c$ synthesised for different particle geometries would thus enable an estimate of the average grain shape in the microstructure. The relationships between $\bar{Q}$ and $\bar{N}_c$ and the aspect ratio* (AR) of elongated hexagonal prisms have been established from computer simulations, see Fig. 2 and eqns (1) and (2). This procedure is discussed in detail in Ref. 12 and 13.

$$AR(\bar{Q}) = 7{\cdot}22 \cdot 10^{-13} e^{39{\cdot}2\bar{Q}} \quad 0{\cdot}732 \le \bar{Q} \le 0{\cdot}771 \quad (1)$$

$$AR(\bar{N}_c) = 3{\cdot}27 \cdot 10^{-6} e^{2{\cdot}58\bar{N}_c} \quad 5{\cdot}146 \le \bar{N}_c \le 5{\cdot}722 \quad (2)$$

2.4 3D reconstruction

The basic idea of the stereological method is that the true β-Si_3N_4 grain size distribution can be represented by a size distribution of hexagonal prisms which all have the same aspect ratio.[12,13] This aspect ratio should be the average aspect ratio determined as described in section 2.3 above.

*The aspect ratio is the ratio between the length and the width of the β-Si_3N_4 grain. A hexagonal prism has two possible widths; a smaller between two opposite prismatic sides and a larger between two opposite corners of the hexagonal cross-section. In this paper the larger width is used for determination of the aspect ratio. The smaller width has frequently been used in the literature for aspect ratio determination. This results in a higher value which can be obtained from the values presented in this paper by multiplying by 1·15.

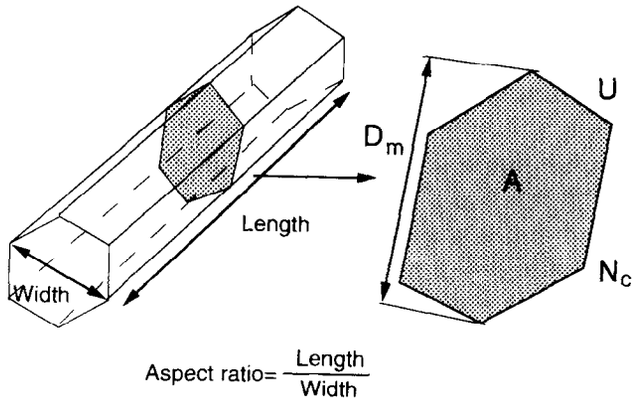

Fig. 1. Elongated hexagonal prism with a polygonal grain section and 2D parameters which can be used to describe the section. D_m, maximum grain section dimension; A, section area; U, perimeter; N_c, number of corners. A dimensionless shape parameter (Q) can be calculated from $Q = 4\pi A/U^2$.

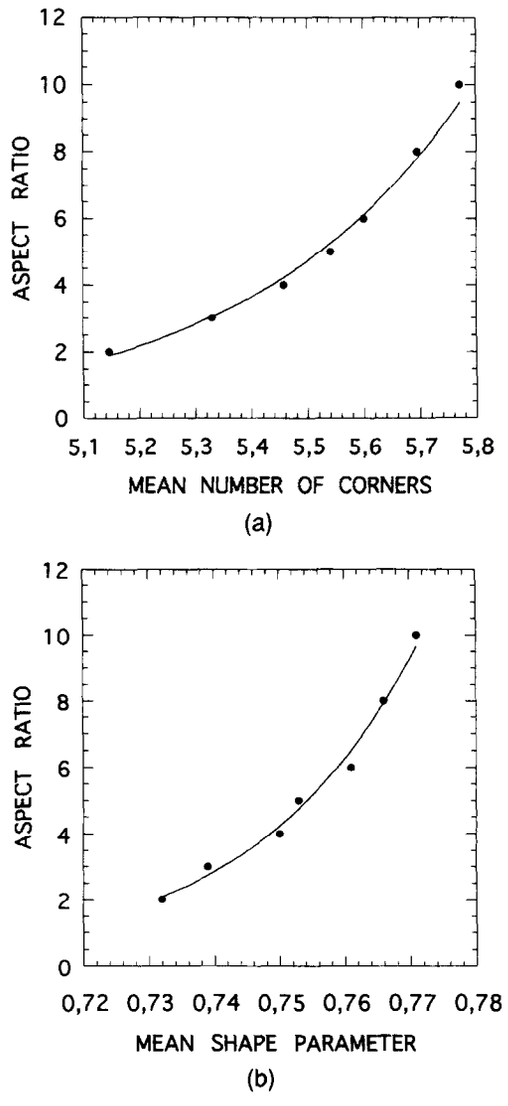

Fig. 2. The aspect ratio as function of the mean values of (a) the shape parameter, $\bar{Q}$, and (b) the number of corners/grain section ($\bar{N}_c$). Data from Ref. 12.

It is possible to computer-synthesise distributions of 2D section parameters from a proposed 3D size distribution of hexagonal prisms with a given aspect ratio.[12,13] The stereological parameters for the hexagonal prism which are required in the synthesising process are obtained from computer simulations as described in Refs 12 and 14. The synthesised distribution of a selected 2D parameter is compared with the experimental distribution of the same parameter. If there is a satisfactory fit between these distributions the proposed 3D size distribution is considered to represent the grain size distribution in the experimental material. An exact grain shape is not a critical parameter for an accurate reconstruction of the 3D size distribution.[15]

The maximum grain section dimension, D_m, is an appropriate 2D parameter for the reconstruction procedure.[12,13] It has previously been shown that it is sufficient to measure 400 grain sections when D_m is used for a 3D reconstruction of this type of microstructure.[12] The reconstruction procedure is described in detail in Refs 12 and 14.

The reconstructed microstructures were described as number of grains with a certain length per unit volume and as volume fractions of grains in length classes. All β-Si_3N_4 grains in a reconstructed microstructure had the same aspect ratio.

2.5 Indentation fracture toughness

The fracture toughness of materials A1, A3, A5, B5, E5 and F5 was determined by the indentation technique, using eqn (3) by Anstis[16]

$$K_{Ic} = 0{\cdot}016 \cdot (E/H)^{1/2} \cdot P/c^{3/2} \qquad (3)$$

where E is the Young's modulus, H the measured hardness, P the Vickers indentation load and c is the crack length measured from the centre of the impression. A load of 40 kg was used for Vickers indentation and E was set to 304 GPa when calculating the fracture toughness from eqn (3). The fracture toughness was determined from five Vickers indentation marks in each material and the precision was given as the 95% confidence interval. Crack propagation was studied by imaging of indentation cracks in the SEM.

3 Results and Discussion

3.1 General observations

3.1.1 Density

The bulk densities of the experimental materials are given in Fig. 3. Compositions C and D with additions of only Al_2O_3 or Y_2O_3 had a significant porosity after all sintering times as shown in Fig. 4. When only Al_2O_3 is added decomposition and volatilisation of Al_2O_3 may occur.[17] It may thus be difficult to sinter the material to closed porosity at the initial stages of the GPS cycle. Materials fabricated with only Y_2O_3 are generally difficult to densify without hot isostatic pressing. The smaller fraction of liquid phase with a high viscosity which forms when Y_2O_3 is added (material D) may otherwise result in an incomplete densification. Al_2O_3 reduces the eutectic temperature when added together with Y_2O_3. Compositions A, B and E appeared to be fully dense after 1 h at 1900°C and did not show any variations in density with time at densification temperature (see Fig. 3) although the microstructures were partly disintegrated after 10 h, Figs 5–7. Composition F required 5 h at the densification temperature in order to reach full density, Fig. 3.

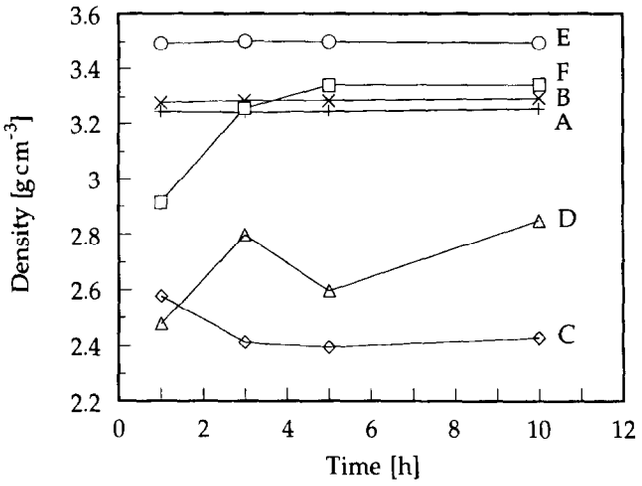

Fig. 3. The bulk densities of the experimental materials as function of time at densification temperature.

Fig. 4. SEM image of a section through material C5 showing the porosity of this material.

3.1.2 Si_3N_4 morphology

X-ray diffraction patterns from materials A1–A10, B5, E5 and F5 did not show any reflections from retained α-Si_3N_4. This implies a complete α- to

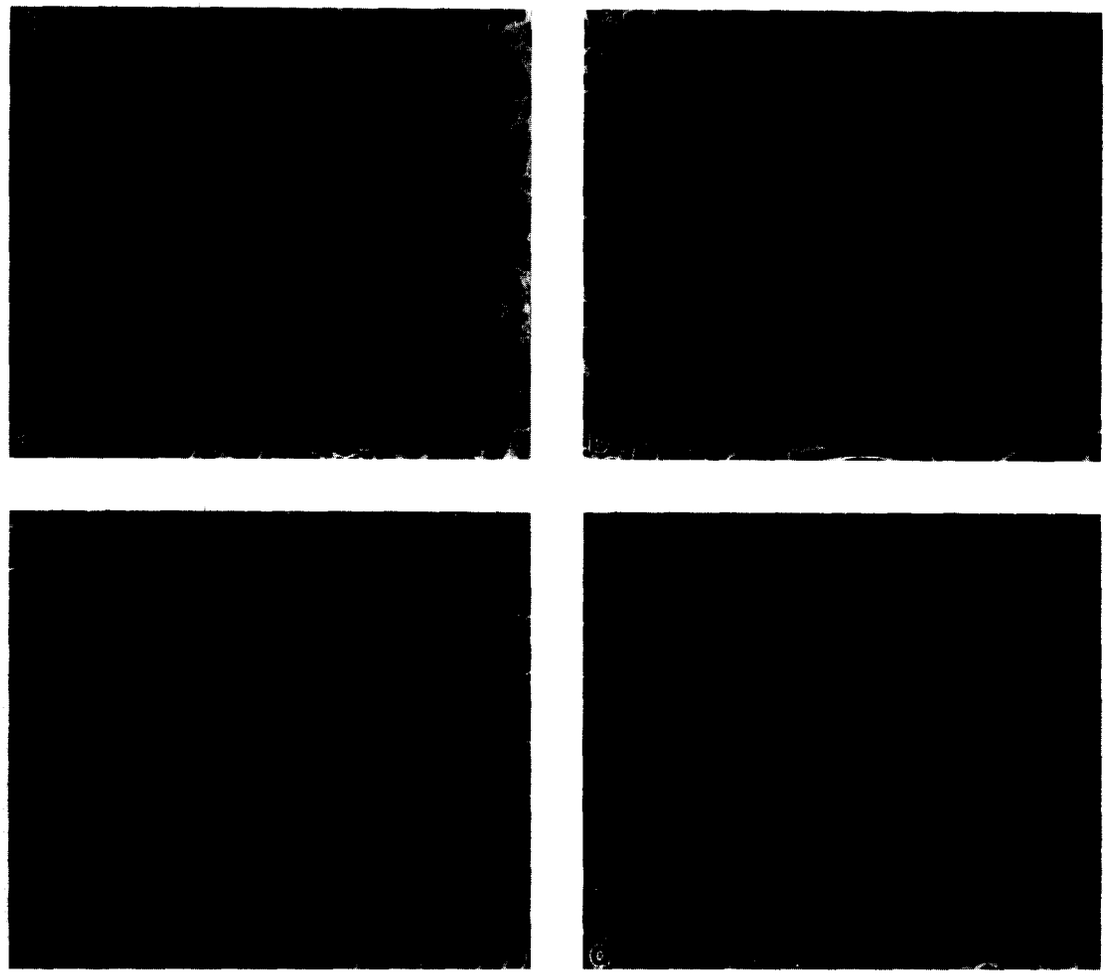

Fig. 5. SEM images of plasma-etched sections through materials with composition A (Y_2O_3/Al_2O_3 = 0·60) after (a) 1, (b) 3, (c) 5 and (d) 10 h at the densification temperature.

β-Si_3N_4 phase transformation during densification. Si_2N_2O, which may form elongated grains that have an appearance similar to β-Si_3N_4 on etched sections, could not be detected by XRD.

SEM of plasma-etched sections showed a large variation in β-Si_3N_4 grain section size and shape, and there was a large intergranular volume fraction in the dense materials, Figs 5–8. Composition A showed a clear increase in grain section area with sintering time, Fig. 5. This relation between grain section area and process time was not so pronounced for composition B and even less obvious for composition E, Figs 6 and 7. The difference between compositions B and E was that E contained Yb_2O_3 instead of Y_2O_3, see Table 1.

The microstructure in material B1 appeared much coarser than that in A1, but this difference between the two compositions became less pronounced after a prolonged time at the densification temperature, Figs 5 and 6. The grain sections in specimen F5 (which had the largest Y_2O_3 addition) appeared larger than those in A5 and B5, and a significant number of elongated grain sections were observed, Fig. 8.

Curved grain boundaries between adjacent β-Si_3N_4 grains and steric hindrance were observed in all microstructures, Fig. 9. Extremely large grain sections were occasionally also found in the microstructures, Fig. 10.

3.1.3 Intergranular microstructure

Secondary crystalline phases were detected in the materials by X-ray diffraction. Al-substituted N-α-wollastonite (Y_2SiAlO_5N) was identified in the specimens with composition A after all sintering times. The relative fraction was determined by the peak height ratio between two Y_2SiAlO_5N peaks and two β-Si_3N_4 peaks according to eqn (4), see Table 2.

$$W = \frac{Y_2SiAlO_5N[(101) + (102)]}{Y_2SiAlO_5N[(101)+(102)]+Si_3N_4[(200)+(101)]} \quad (4)$$

Y_2SiAlO_5N was also identified in material B5 and the relative fraction was determined to be 0·054 by eqn (4).

The Al-substituted N-α-wollastonite forms by glass devitrification, and has been reported to be unstable above 1100°C.[18] This implies that the

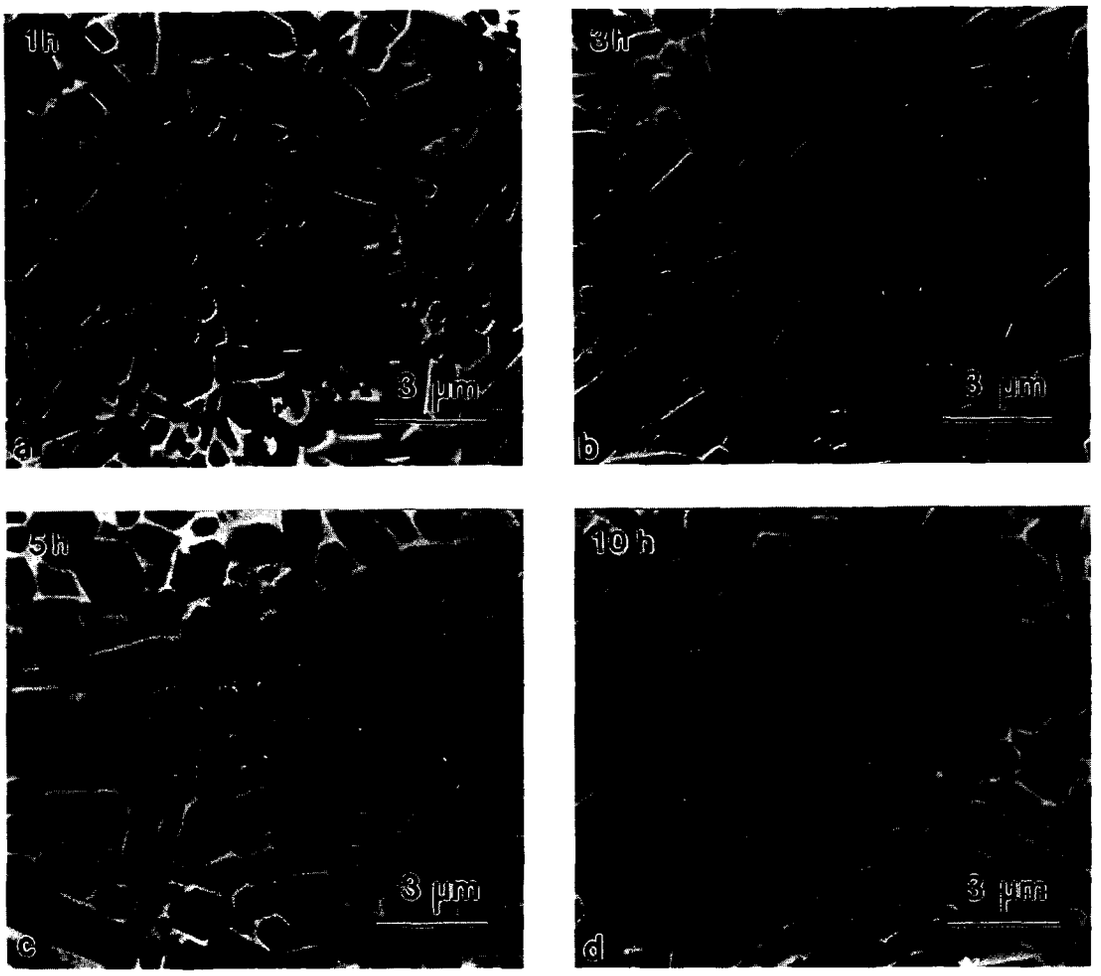

Fig. 6. SEM images of plasma-etched sections through materials with composition B (Y_2O_3/Al_2O_3 = 1·38) after (a) 1, (b) 3, (c) 5 and (d) 10 h at the densification temperature.

Y_2SiAlO_5N formed during cooling from the densification temperature and did, thus, not affect β-Si_3N_4 grain growth to any significant extent.

It can be noted that the amount of Y_2SiAlO_5N in materials with composition A increased with time at densification temperature (Table 2). Crystallisation of pockets of residual glass is not only dependent upon the composition of the glass. Theoretical and experimental work has shown that a certain volume of the pocket is required in order for crystallisation to be energetically favourable.[19,20] This could be one reason for the observed increase in the wollastonite content in the A materials with time at densification temperature; the intergranular phase was concentrated to larger intergranular pockets when the β-Si_3N_4 grain sections became larger, see Figs 5–7. This would, hence, favour crystallisation during cooling. A more homogenous liquid phase composition close to the wollastonite may also develop after longer times at high temperature. The increased fraction of N-α-wollastonite in material B5 compared to A5 can be explained by a higher Y content and larger intergranular pockets at multigrain junctions.

The higher Y_2O_3 addition in F5 resulted in the formation of the more Y-rich N-YAM phase ($Y_{10}Al_2Si_3O_{18}N_4$). The N-YAM has its melting point between 1900 and 2000°C[18] and may thus crystallise at the densification temperature. Hence, the formation of N-YAM might affect β-Si_3N_4 grain growth.

The secondary crystalline phase(s) in material E5 which was densified with Yb_2O_3, instead of Y_2O_3, together with Al_2O_3 could not be conclusively determined. However, the positions of the reflections in the X-ray diffractogram suggested that a Yb-containing phase with a crystal structure similar to the N-YAM phase, which in this case would have the chemical formula $Yb_{10}Al_2Si_3O_{18}N_4$, was present in the microstructure of material E5. $Yb_{10}Al_2Si_3O_{18}N_4$ has previously been suggested to form in a Si_3N_4 ceramic with additions of Yb_2O_3 and Al_2O_3.[21] After sintering at 1800°C for 30 min a major part of the intergranular structure had crystallised to this phase.[21] If $Yb_{10}Al_2Si_3O_{18}N_4$ is stable up to 1900°C, as is the corresponding Y-containing N-YAM phase, it may form during densification and affect β-Si_3N_4 grain growth. However, the identification of this phase was associated with some uncertainty both in the present investigation and in Ref. 21.

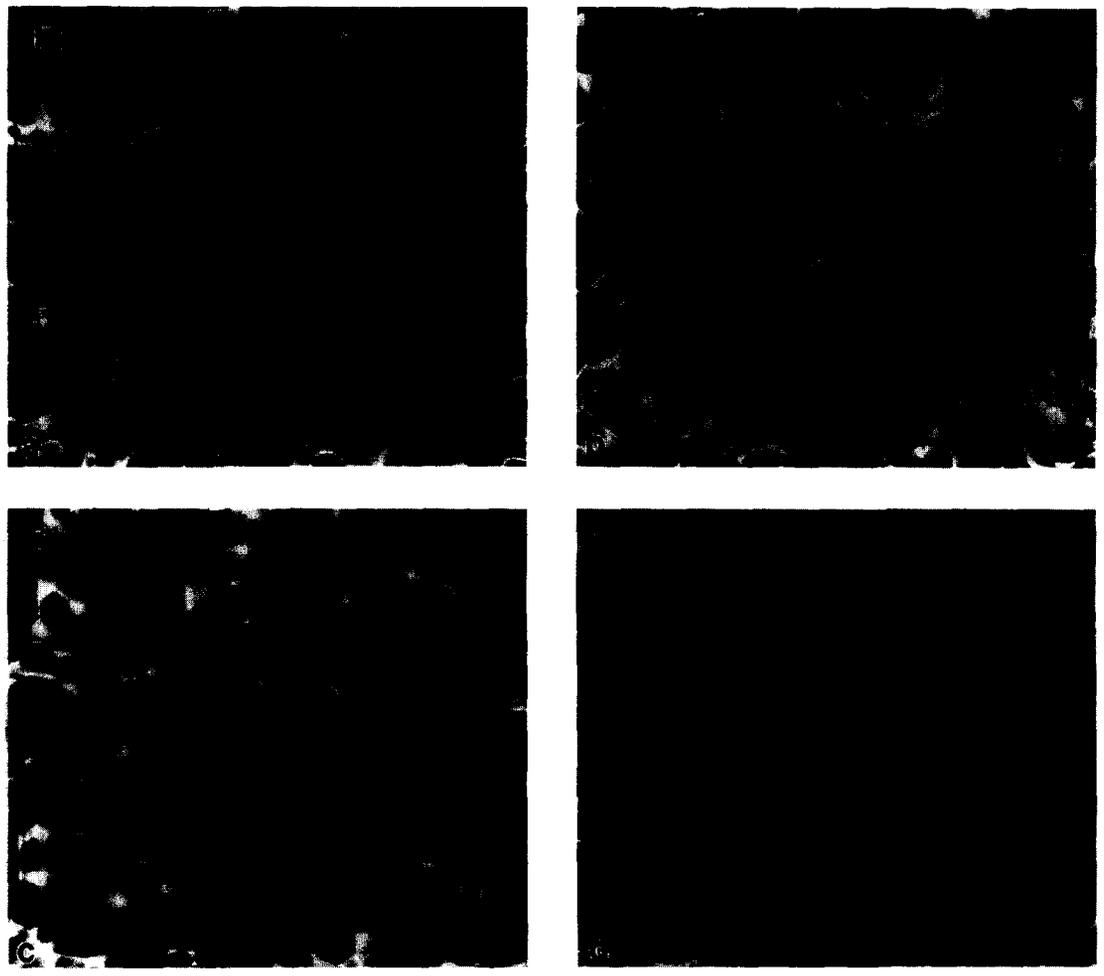

Fig. 7. SEM images of plasma-etched sections through materials with composition E (Yb_2O_3/Al_2O_3 = 1·38) after (a) 1, (b) 3, (c) 5 and (d) 10 h at the densification temperature.

3.2 Microstructural reconstruction

3.2.1 Quantitative microscopy

The mean values of the 2D parameters determined from quantitative microscopy are given in Table 3. The precision of $\bar{D}_m$ and $\bar{A}$ are given as the 95% confidence interval. The mean values of maximum grain section dimension, $\bar{D}_m$, and area, $\bar{A}$, of the materials with composition A increased with processing time. An increased Y_2O_3/Al_2O_3 ratio in the starting powder mixture also resulted in higher values of $\bar{D}_m$ and $\bar{A}$. This is in accordance with the general SEM observations in Figs 5–9.

The plot of $\bar{Q}$ as function of number of measured grain sections, see Fig. 11, shows that $\bar{Q}$ is dependent upon the overall chemistry. An increased Y_2O_3/Al_2O_3 molar ratio from 0·60 to 1·38 (specimens A5 and B5) resulted in an increased $\bar{Q}$, and $\bar{Q}$ increased further when the Y_2O_3 in composition B was replaced by Yb_2O_3 (specimens B5 and E5). These differences imply that the β-Si_3N_4 grains in these materials had different aspect ratios. $\bar{N}_c$ showed a similar behaviour, see Table 3. A further increase in the relative Y_2O_3 content (specimen F5) resulted in decreased $\bar{Q}$ and $\bar{N}_c$ values. Smaller variations in $\bar{Q}$ and $\bar{N}_c$ with sintering time were also observed for composition A.

The mean aspect ratios determined for the different microstructures by eqns (1) and (2) are given in Table 4. It can be noted that the β-Si_3N_4 aspect ratio seems to be dependent upon the overall composition; an increased Y_2O_3/Al_2O_3 ratio as well as the replacement of Y_2O_3 by Yb_2O_3 resulted in an

Fig. 8. SEM image of a plasma-etched section through material F5 (Y_2O_3/Al_2O_3 = 8·5).

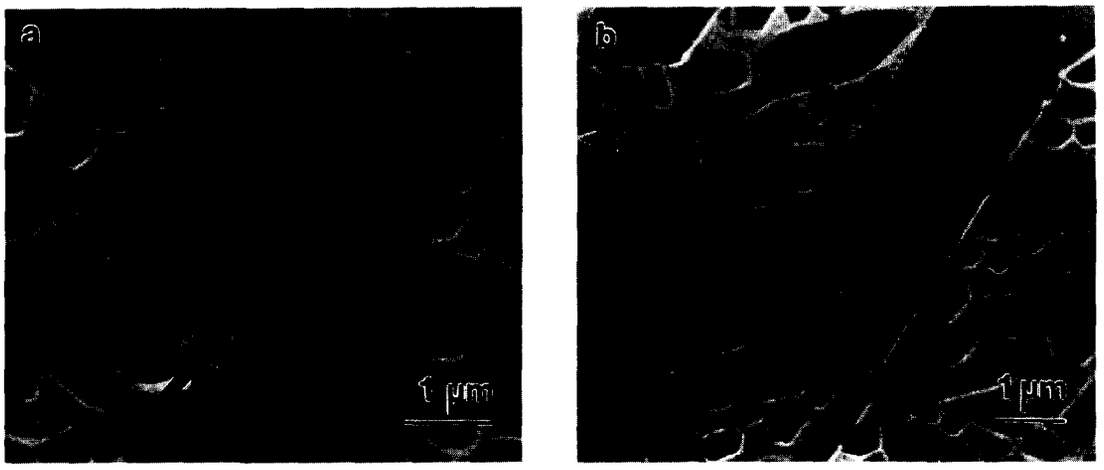

Fig. 9. (a) Curved grain boundary between adjacent β-Si_3N_4 grains (arrowed) in material A5. (b) Steric hindrance of larger β-Si_3N_4 grain by smaller grains in material A5. Curved grain boundaries can also be observed. All grain boundaries contained intergranular films.

increased mean aspect ratio (specimens A5, B5 and E5). There was, however, no obvious trend when the time at the densification temperature was increased (specimens A1, A3 and A5). The aspect ratio of individual β-Si_3N_4 grains may, however, vary due to variations in the local chemistry and steric hindrance. The microstructure of F5 had a pronounced fibrous appearance in the SEM (Fig. 8) but the evaluation of data from quantitative microscopy gave a mean aspect ratio of only 1·8 (from $\bar{Q}$) or 4·5 (from $\bar{N}_c$).

3.2.2 3D grain size distributions

The value of $\bar{Q}$ would be less sensitive than $\bar{N}_c$ to deviations in grain shape caused by steric hindrance, particularly after prolonged time at densification temperature. The aspect ratios for the 3D reconstructions were therefore determined from $\bar{Q}$. Deviations from the derived ideal grain shape are, however, not determining for the reconstruction of the 3D grain size distribution.[15] A hexagonal prism with aspect ratio 3[†] was chosen as the average grain shape for the 3D reconstruction of the grain size distributions in materials A1, A3, and A5. Hexagonal prisms with aspect ratios 5, 6 and 2 were chosen for the 3D reconstructions of the microstructures of specimens B5, E5 and F5, respectively.

The reconstructed 3D β-Si_3N_4 grain size distributions are shown in Fig. 12, and mean grain volume, mean grain length and number of grains/unit volume obtained from these distributions are given in Table 5.

[†]$\bar{Q}$ indicated, however, that the mean aspect ratio was closer to 2 rather than 3 in material A3. Since the experimental distribution of Q was closer to the theoretical Q distribution for a prism of aspect ratio 3 it was assumed that 3 was an appropriate aspect ratio also for the reconstruction of the microstructure of material A3.

An increased processing time of materials with composition A led to a larger mean grain size and also to a broader grain size distribution. The reconstructed grain size distributions of the materials formed with additions of Y_2O_3 and held 5 h at the densification temperature (materials A5, B5 and F5) are all comparatively broad; there is a fraction of larger β-Si_3N_4 grains in these distributions, see Fig. 12.

Replacement of Y_2O_3 in composition B by Yb_2O_3 (composition E) resulted in a more narrow grain size distribution but a significantly larger mean grain volume after 5 h at the densification temperature, see Fig. 12 and Table 5. This suggests that Yb_2O_3 promotes the formation of a more stable β-Si_3N_4 grain morphology.

An increased relative Y_2O_3 content of the starting powder mixture (materials A5 and B5) resulted in a higher average aspect ratio and a reduced number of grains per unit volume, but in a virtually unchanged mean grain volume, see Table 5. The use of Yb_2O_3 instead of Y_2O_3 resulted in a further

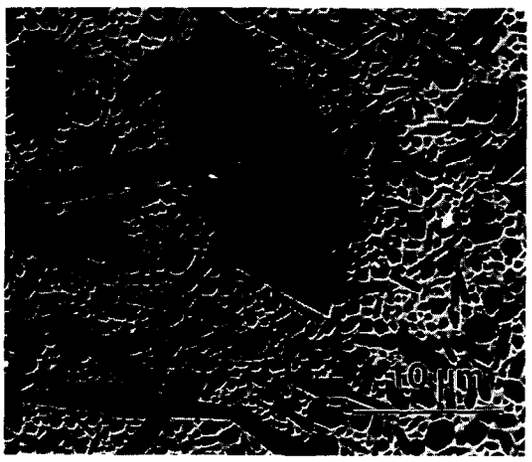

Fig. 10. An extremly large β-Si_3N_4 grain section observed in material A5.

Table 2. Relative fraction (W) of Y_2SiAlO_5N in materials of composition A

Time (h)	*1*	*3*	*5*	*10*
W	0·014	0·033	0·045	0·058

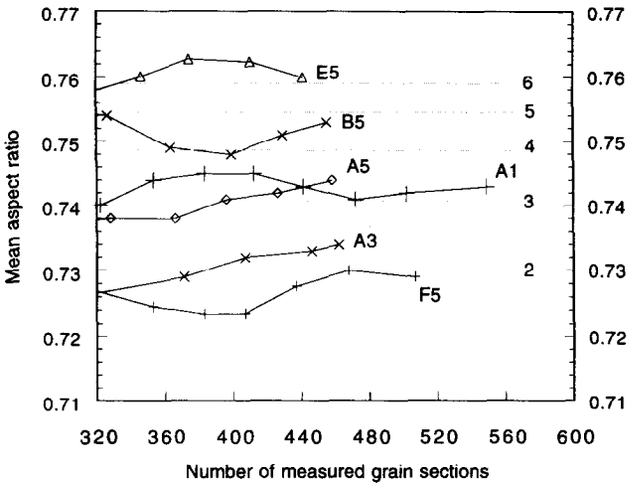

Fig. 11. The mean values of the shape parameter, $\bar{Q}$, as function of number of measured grain sections for materials A1, A3, A5, B5, E5 and F5.

increased average aspect ratio and also in a significantly increased mean grain volume and, consequently, in a reduced number of grains per unit volume (see data for specimens B5 and E5 in Table 5).

The molar fractions of α- and β-Si_3N_4 and metal oxides were kept constant in the starting powder mixtures in the present investigation. The results show that the β-Si_3N_4 grain shape and the number of grains per unit volume in the sintered material are governed by the chemistry of the liquid phase sintering medium (see results for materials A5 and B5/E5 in Table 5). This is in contrast to previous work which suggested that nucleation and growth occur predominantly on pre-existing β-particles, and that the final grain size distribution in β-Si_3N_4 materials is nearly exclusively determined by the number and size distribution of β-particles in the starting powder compact.[22]

The low mean aspect ratio determined for material F5 was unexpected and the reconstructed grain size distribution using an aspect ratio of 2 was extremely broad, see Fig. 12. These results might indicate that a high relative Y_2O_3 content resulted in a fraction of larger elongated β-grains in a matrix of smaller grains with a lower aspect ratio.[23] However, the low aspect ratio may also be a misleading result due to development of a non-random distribution of the β-grains; larger elongated grains may be aligned in the microstructure,[24] and such texturing would affect the experimental $\bar{Q}$ and $\bar{N}_c$. This stereological method can be applied only to isotropic microstructures.

3.3 β-Si_3N_4 grain growth

3.3.1 Effect of time at densification temperature

Figure 13 shows the reconstructed 3D grain size distributions for materials A1–5 in the form of volume fractions of β-Si_3N_4 grains in different length classes. The microstructure consisted mainly of two size fractions of β-Si_3N_4 grains after 1 and 3 h at the final densification temperature, while a prolonged densification time (5 h) resulted in a more spread-out grain size distribution.

Grain growth kinetics by liquid phase sintering usually follows eqn (5),

$$\bar{d}^n - \bar{d}_0^n = Kt \qquad (5)$$

where $\bar{d}$ is the mean particle diameter, n is the growth exponent, K is the growth rate constant and t is time.[25] Figure 14 shows the logarithmic values of mean grain length as function of logarithmic values of sintering time for materials with composition A. The slope of the curve was determined to be 0·31 which is equal to a growth exponent of 3·2 in eqn (5).

3.3.2 Grain growth models

Curved grain boundaries containing thin glassy films were frequently observed in these microstructures, Fig. 9. These features suggest that the larger β-grain is growing at the expense of the smaller grain in a process of coalescence, Fig. 16. At coalescence, adjacent grains of different size grow into one single grain by a continuous process of directed grain growth and reshaping.[25] Grain boundaries would move towards their centre of curvature during coalescence, and the

Table 3. Number of measured grain sections (N) and mean values of maximum grain section dimension ($\bar{D}_m$) grain section area ($\bar{A}$), shape parameter ($\bar{Q}$), and number of corners/grain section ($\bar{N}_c$)

Material	N	$\bar{D}_m$ *[μm]*	$\bar{A}$*[(μm)²]*	$\bar{Q}$	$\bar{N}_c$
A1	549	0·59 ± 0·05	0·19 ± 0·03	0·743	5·25
A3	462	0·95 ± 0·09	0·50 ± 0·11	0·734	5·31
A5	570	1·09 ± 0·09	0·65 ± 0·12	0·744	5·39
B5	455	1·28 ± 0·11	0·86 ± 0·15	0·753	5·56
E5	441	1·23 ± 0·09	0·77 ± 0·09	0·760	5·66
F5	507	1·42 ± 0·11	1·00 ± 0·16	0·729	5·47

Table 4. Average aspect ratios of the β-Si_3N_4 grains in the experimental materials

Material	*Average aspect ratio determined from:*	
	$\overline{Q}$	$\overline{N}_c$
A1	3·2	2·5
A3	2·3	2·9
A5	3·3	3·5
B5	4·8	5.5
E5	6·3	7·1
F5	1·9	4·4

migration would, in these materials, occur by a dissolution/reprecipitation process via the liquid grain boundary film.

The observed formation of a fraction of larger β-Si_3N_4 grains during prolonged densification time is consistent with an increased probability for coalescence with increasing grain size.[26,27] It is thus suggested that β-Si_3N_4 grain coarsening to a significant extent occurs by coalescence. Observations indicating β-Si_3N_4 grain coalescence have also been reported previously.[28] However, concurrent Ostwald ripening may also take place in the presence of larger liquid volumes.

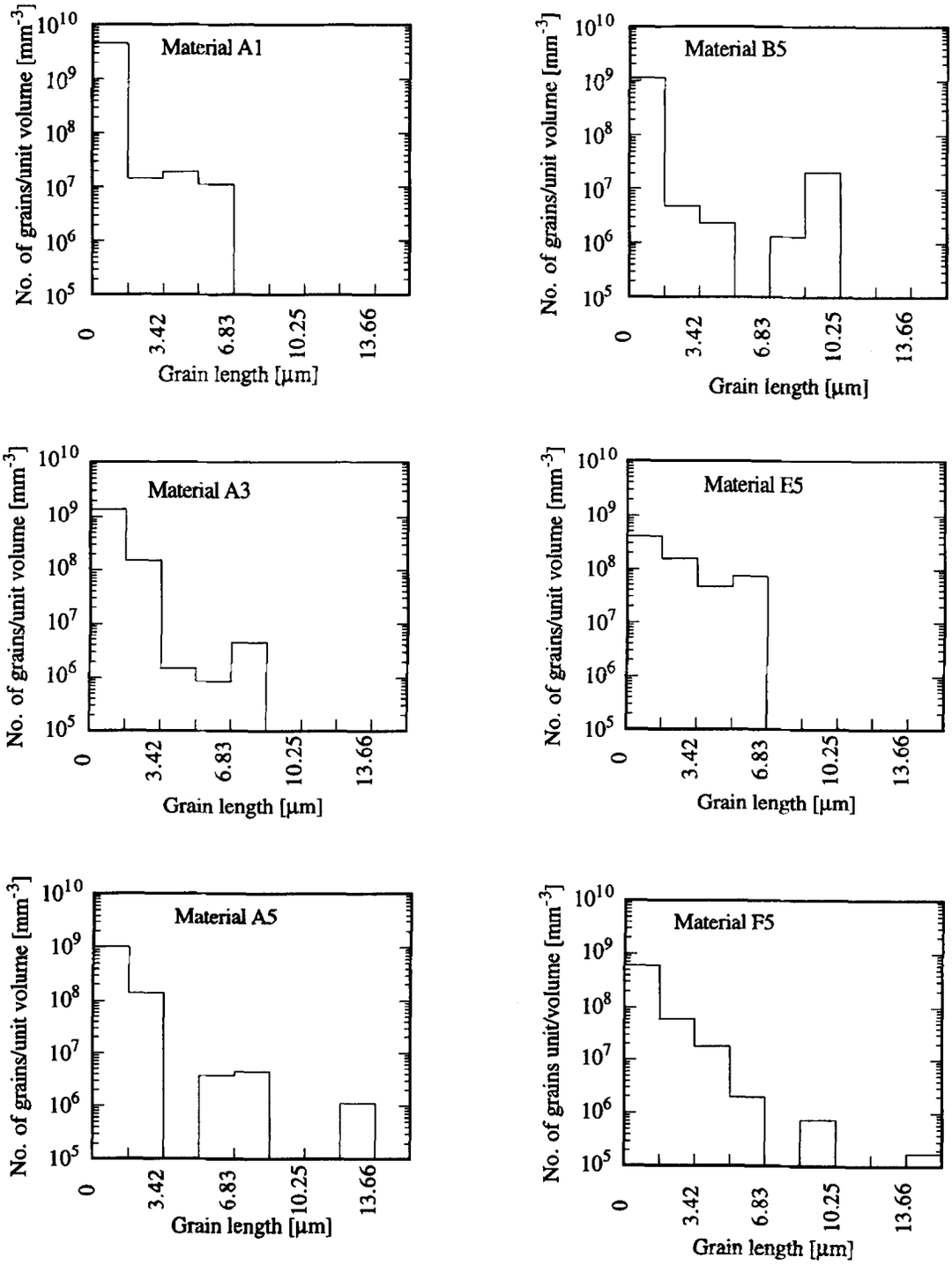

Fig. 12. Reconstructed 3D grain size distributions.

Table 5. Mean values obtained from the reconstructed β-Si_3N_4 grain size distributions

Material	*Aspect ratio used in 3D reconstruction*	*Mean grain volume (μm^3)*	*Mean grain length (μm)*	*Grains/unit volume (10^9 mm^{-3})*
A1	3	0·11	1·14	4·71
A3	3	0·27	1·55	1·53
A5	3	0·49	1·90	1·19
B5	5	0·47	2·63	0·90
E5	6	0·67	3·33	0·68
F5	2	0·87	1·75	0·68

The grain growth exponent was determined to be $n = 3{\cdot}2$ for composition A. This value was calculated from only three grain size distributions, but is in fair agreement with reported values in the literature. Hwang and Tien reported that both length and width of β-Si_3N_4 grains grow according to $n = 3$.[28] Lai and Tien reported the growth exponent to be 3 in the β-grain length direction and 5 in the width direction.[29]

A grain growth exponent of 3 implies that transport of species in the liquid is the rate controlling step. Tokayo, Kaysser and Petzow have analysed grain growth during liquid phase sintering when particle coalescence is the basic growth mechanism.[26,27] When coalescence is controlled by diffusion through a liquid the growth exponent was postulated to be $n = 3$. A growth exponent of 3 indicates also according to the Lifshitz–Slyozov–Wagner (LSW) model of Ostwald ripening that the rate controlling step is diffusion through the liquid phase; a growth exponent of 2 would indicate that the process is controlled by the rate of reaction at the interface between the particle and the liquid.[30,31]

The present results, obtained by the stereological method discussed in detail in Ref. 12, thus lend support to earlier work which implied that the rate controlling step during α- to β-Si_3N_4 transformation and β-Si_3N_4 grain growth is diffusion of Si and N through the liquid phase.[29,32]

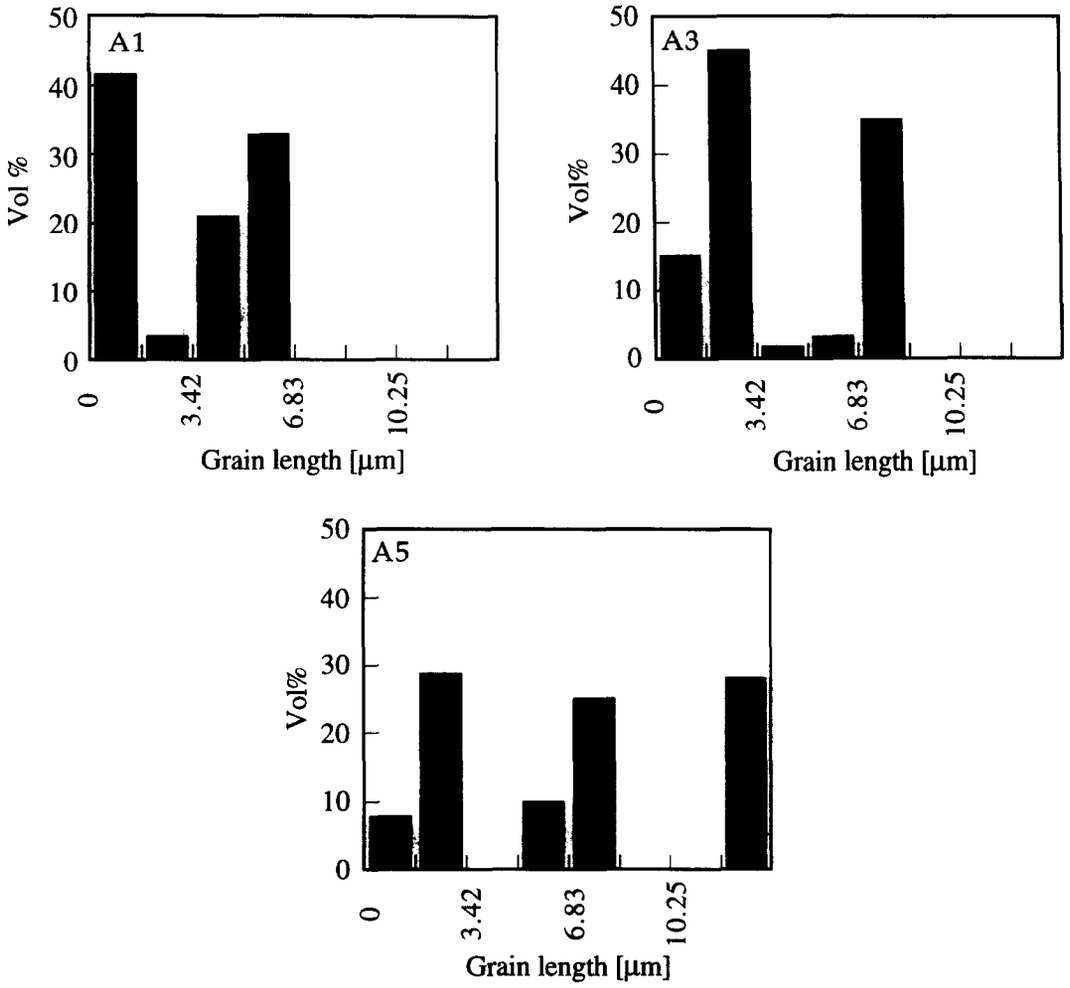

Fig. 13. The reconstructed grain size distributions of materials A1, A3 and A5 expressed as volume fractions of the total β-Si_3N_4 grain volume.

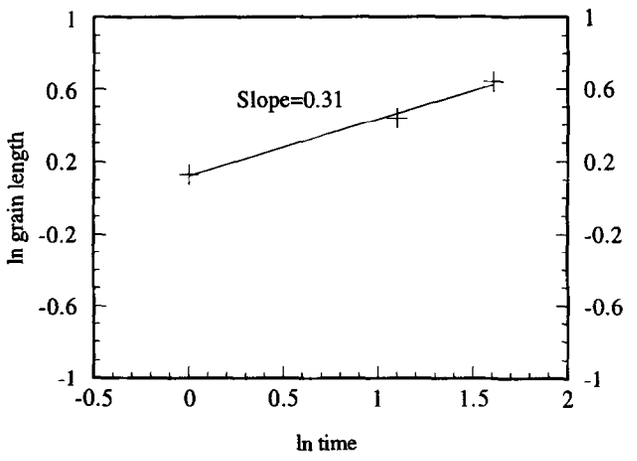

Fig. 14. Logarithm of the mean grain length as function of logarithm of time at densification temperature for materials A1, A3 and A5.

3.3.3 Effect of Y_2O_3/Al_2O_3 molar ratio

The grain sections in material A1 were significantly smaller than in B1, see Figs 4 and 5. This indicates, provided that the average aspect ratios do not change with time at densification temperature, that the β-Si_3N_4 grain size was smaller in A1 than in B1.

The oxide content of starting powder composition A is approximately on the tie line of the compatibility triangle with a lowest eutectic temperature of 1385°C in the Y_2O_3–Al_2O_3–SiO_2 system.[33] The higher Y_2O_3 content of composition B moves the overall oxide composition into an adjacent compatibility triangle with a lowest eutectic temperature of 1400°C. (It has been indicated that the presence of N lowers these eutectic temperatures.[1]) The formation of the liquid phase sintering medium in these materials will thus take place during heating to the densification temperature. However, the liquid formation would presumably start at a lower temperature in green bodies with composition A, and this liquid would also have a lower viscosity. Liquid formation early in the sintering cycle will allow more time for homogenous β-Si_3N_4 nucleation, and thereby result in a larger number of nuclei. This would also result in a smaller grain size if the sintering process is interrupted after shorter times at the final densification temperature.

It is hence suggested that an increased liquidus temperature, brought about by an increased Y_2O_3/Al_2O_3 ratio of the starting powder composition, will reduce the β-Si_3N_4 nucleation density, and thereby result in an initially coarser grain structure. There was no pronounced dependence of grain size upon Y_2O_3/Al_2O_3 ratio after a prolonged time at densification temperature; specimens A5 and B5 had the same mean grain volume. This suggests that the reduced viscosity of a more Al_2O_3-rich liquid promotes diffusion in the liquid phase and thereby grain growth.

3.4 Relation between microstructure and indentation fracture toughness

Grain growth in materials with composition A did initially result in an increased toughness, see Table 6. The contribution from crack-bridging and grain pull-out to fracture toughness is expected to increase with grain diameter while the contribution from crack-deflection is expected to increase with aspect ratio.[10,11] Provided that the average aspect ratio does not change with time at densification temperature, this implies that the major toughening mechanisms in materials A1 and A3 are bridging and pull-out.

Specimen A5 had, however, a lower toughness than A3, despite the increased mean grain diameter, and there was a significant scatter in the measurements. The amount of wollastonite in materials with composition A increased with time at densification temperature. The crystallisation of residual glass may introduce stresses in the material; a reduction in specific volume would result in tensile stresses across wollastonite/β-Si_3N_4 boundaries. Such stresses would weaken the interface and thereby promote crack propagation and give the material a reduced fracture toughness.

Specimen B5 had a lower fracture toughness than A5 despite a higher mean aspect ratio. However, the mean grain volume in these materials was the same which indicates that B5 had a smaller mean grain diameter. The lower indentation fracture toughness of specimen B5 would, hence, be consistent with the argument that a smaller grain diameter would reduce toughening caused by bridging and pull-out.[11] In addition, B5 had a higher wollastonite content than A5.

The data on indentation fracture toughness together with the reconstructed microstructures and the results from quantitative microscopy hence suggest that bridging and pull-out of β-Si_3N_4 grains are the major toughening mechanisms in the materials formed with Y_2O_3. This is in agreement with observations in the SEM; cracks from the indentation marks were predominantly intergranular, Fig. 15, and bridging of the cracks by β-Si_3N_4 grains or volumes of grains was observed.

Table 6. Indentation fracture toughness

Material	K_{IC} *(MPa m$^{1/2}$)*
A1	6·6 ± 0·4
A3	9·8 ± 0·4
A5	7·3 ± 0·9
B5	5·9 ± 0·4
E5	4·1 ± 0·5
F5	6·1 ± 0·6

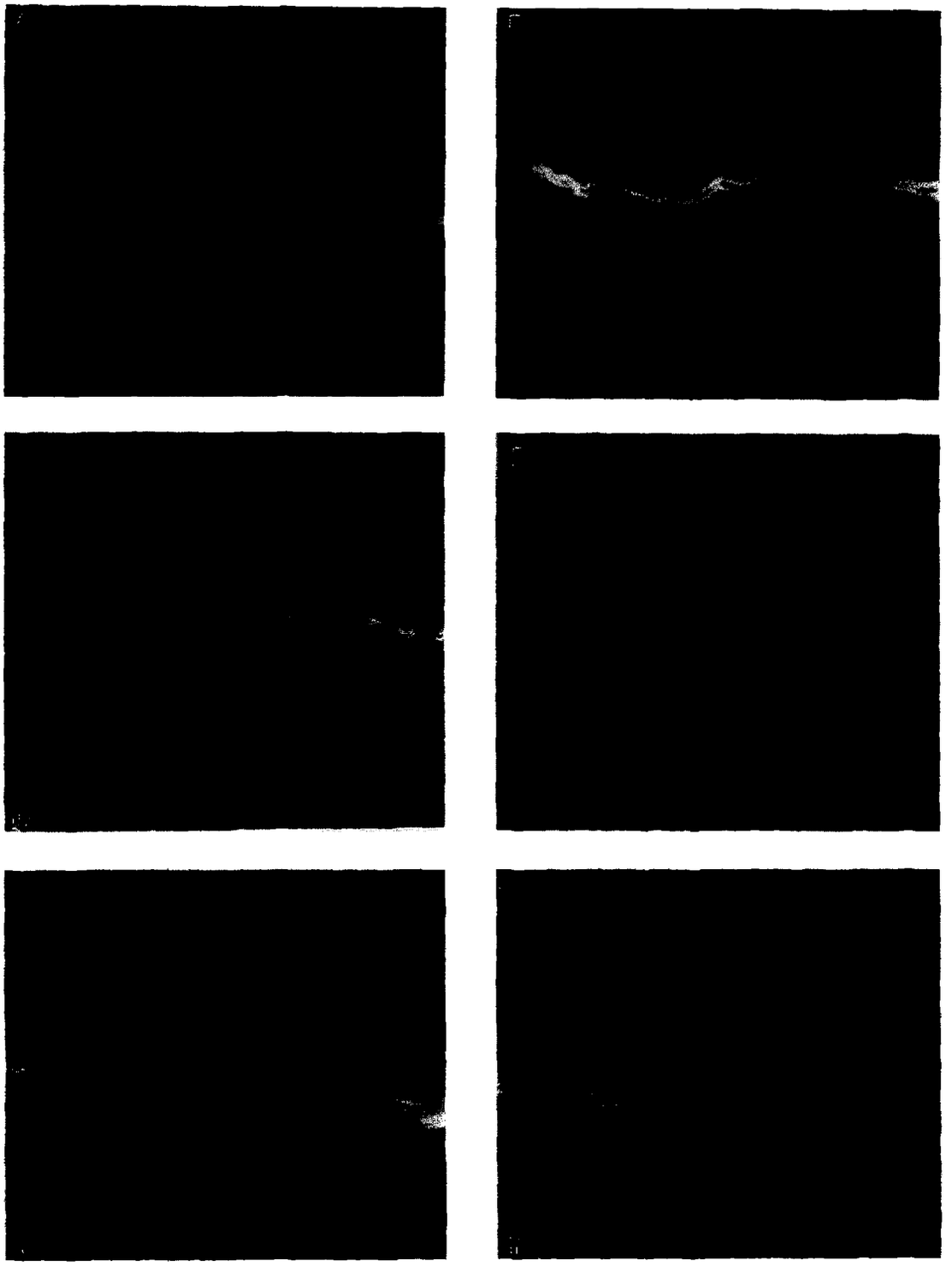

Fig. 15. SEM images of Vickers indentation cracks in materials (a) A1, (b) A3, (c) A5, (d) B5, (e) E5 and (f) F5. The arrows indicate the direction of crack propagation.

The contribution from different toughening mechanisms will, however, also depend upon the strength of the β-Si_3N_4/β-Si_3N_4 grain boundaries; a sufficiently weak boundary is a necessary requirement for bridging and pull-out and crack deflection.[11,34] Whether a crack propagates along an inclined β-Si_3N_4 grain boundary resulting in debonding or through a β-grain is dependent upon the ratio between the interface and grain fracture energies as well as the angle between the crack and the β-Si_3N_4 grain.[34]

There was no clear effect of toughness when the Y_2O_3 content of the starting powder was further increased, specimen F5. Crack deflection in this material was observed only when the angle between the crack and the β-grains was comparatively low, Fig. 15.

The low K_{IC} of specimen E5 is consistent with the results from SEM which showed mainly planar and transgranular crack propagation, Fig. 15. The β-grain size and shape would suggest a higher K_{IC} than that determined. This indicates that the

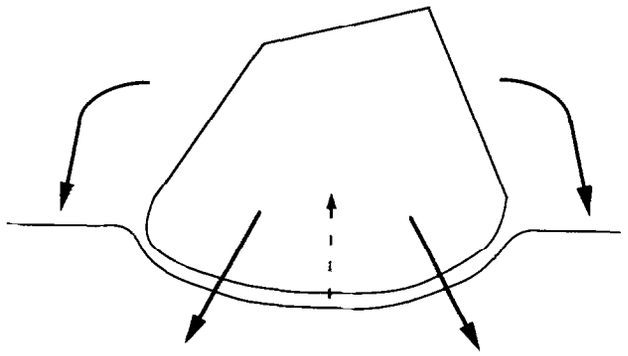

Fig. 16. Coalescence by diffusion through the liquid phase. The black arrows indicate material transport by solution-diffusion-reprecipitation. The dashed arrow indicates migrating direction of the grain boundary.

formation of $Yb_{10}Al_2Si_3O_{18}N_4$ resulted in strong bonding and a stress state that reduced fracture toughness.

5 Conclusions

The application of the stereological method described in Ref. 12 has demonstrated that:

1. The chemistry of the oxynitride liquid phase sintering medium affects β-Si_3N_4 grain shape. An increased Y_2O_3/Al_2O_3 ratio in the starting powder mixture results in an increased average β-Si_3N_4 aspect ratio. The replacement of Y_2O_3 by Yb_2O_3 increases the average aspect ratio further.
2. The chemistry of the liquid affects the β-Si_3N_4 grain size distribution at early stages of densification. A higher relative Al_2O_3 content results in a smaller mean grain size. Grain growth during prolonged holding time at the densification temperature reduces the influence of the Y_2O_3/Al_2O_3 ratio on the mean grain size.
3. Replacement of Y_2O_3 by Yb_2O_3 results in a more narrow grain size distribution with a higher mean grain volume.
4. β-Si_3N_4 grain growth is rate controlled by diffusion through the liquid phase and occurs to a significant extent by coalescence.
5. The combination of metal oxide additives as well as the densification time can be used to 'design' the β-Si_3N_4 grain morphology.
6. Fracture toughness depends both on β-Si_3N_4 grain morphology and the intergranular structure.

Acknowledgements

This project was supported by the Swedish Research Council for Engineering Science (TFR). The experimental materials were fabricated at the Japan Fine Ceramics Center (JFCC), Nagoya.

References

1. Hampshire, S. and Jack, K. H., The kinetics of densification and phase transformation of nitrogen ceramics. In *Special Ceramics 7*, ed. D. Taylor and P. Popper. British Ceramic Research Association, Stoke-on Trent, 1981, pp. 37–49.
2. Wötting, G., Kanka, G. and Ziegler, G., Microstructural development, microstructural characterization and relation to mechanical properties of dense silicon nitride. In *Non-oxide Technical and Engineering Ceramics*, ed. S. Hampshire. Elsevier Applied Science, London, 1986 pp. 83–96.
3. Knutson-Wedel, E. M., Falk, L. K. L., Björklund, H. and Ekström, T., Si_3N_4 ceramics formed by HIP using different oxide additions—Relation between microstructure and properties. *J. Mater. Sci.*, 1991, **26**, 5575–5584.
4. Pyzik, A. J. and Beaman, D. R., Microstructure and properties of self-reinforced silicon nitride. *J. Am. Ceram. Soc.*, 1993, **76**, 2737–2744.
5. Goto, Y. and Thomas, G., Microstructure of silicon nitride ceramics sintered with rare-earth oxides. *Acta Metall. Mater.*, 1995, **43**, 923–930.
6. Ekström, T. and Nygren, M., SiAlON ceramics, *J. Am. Ceram. Soc.*, 1992, **75**(2), 259–276.
7. Falk, L. K. L., Shen Z-J. and Ekström, T., α-β Sialon ceramics in the Dy–Si–Al–O–N and Sm–Si–Al–O–N systems. In *Fourth Euro Ceramics, Vol. 2*, ed. C. Galassi.. Gruppo Editorale Faenza Editrice S.p.A, Faenza, 1995, pp. 163–168.
8. Lange, F. F., Silicon nitride polyphase systems: Fabrication, microstructure and properties. *Int. Met. Rev.*, 1980, No. 1, 1–20.
9. Lewis, M. H. and Lumby, R. J., Nitrogen ceramics, liquid phase sintering. *Powder Metallurgy*, 1983, **26**(2), 73–89.
10. Faber, K.T. and Evans, A. G., Crack deflection processes –II. Experiment. *Acta Met.*, 1983, **67**, 577–584.
11. Becher, P. F., Lin, H. T., Hwang, S. L., Hoffmann, M. J. and Chen, I-W., The influence of microstructure on the mechanical behaviour of silicon nitride ceramics. In *Silicon Nitride Ceramics — Scientific and Technological Advances*, ed. I-W. Chen, P. F. Becher, M. Mitomo, G. Petzow and T-S. Yen. Materials Research Society, Pittsburgh, 1993, pp. 147–158.
12. Björklund, H., Wasén, J. and Falk, L. K. L., Quantitative microscopy of β-Si_3N_4 ceramics. *J. Am. Ceram. Soc.*, in press.
13. Björklund, H., Falk, L. K. L. and Wasén, J., Determination of grain morphology in β-Si_3N_4 ceramics. In *Fourth Euro Ceramics, Vol. 3*, ed S. Meriani and V. Sergo. Gruppo Editorale Faenza Editrice S.p.A, Faenza, 1995, pp. 17–24.
14. Wasén, J. and Warren, R., Quantitative metallographic characterization of cubo-spherical particles. *Metallography*, 1987, **20**, 431–449.
15. Wasén, J. and Warren, R., The influence of the unit particle shape on computer modelling based three dimensional microstructural analysis. Internal report R541/87, Dept. of Engineering Metals, Chalmers University of Technology, Göteborg, 1987.
16. Anstis, G. R., Chantikul, P., Lawn, B. R. and Marshall, D. B., A critical evaluation of indentation techniques for measuring fracture toughness: Direct crack measurements. *J. Am. Ceram. Soc.*, 1981, **64**(9) 533–538.
17. Hirosaki, N., Okada, A. and Akimune, Y., Gas-pressure sintering of silicon nitride containing small amounts of oxide additives. *J. Mater. Sci. Lett.*, 1990, **9** 1322–1323.
18. Jack, K. H., Sialons: A study in materials development. In *Non-Oxide Technical and Engineering Ceramics*, ed. S. Hampshire. Elsevier Applied Science, London, 1986, pp. 1–30.

19. Raj, R. and Lange, F. F., Crystallization of small quantities of glass (or liquid) segregated in grain boundaries. *Acta Met.*, 1981, **29**, 1993–2000.
20. Falk, L. K. L. and Dunlop, G. L., Crystallisation of the glassy phase in a Si_3N_4 material by post sintering heat treatments. *J. Mater. Sci.*, 1987, **22**, 4369–4374.
21. Vetrano, J. S., Kleebe, H-J., Hampp, E., Hoffmann, M. J. and Cannon, R. M., Epitaxial deposition of silicon nitride during post-sintering at heat treatment. *J. Mater. Sci. Lett.*, 1992, **11**, 1249–1252.
22. Dressler, W., Kleebe, H.-J., Hoffmann, M. J., Rühle, M. and Petzow, G., Model experiments concerning abnormal grain growth in silicon nitride. *J. Eur. Cer. Soc.*, 1996, **16**, 3–14.
23. Handwerker, C. A., Wallace, J. S., Foecke, T. J., Kattner, U. R. and Blendell, J. E., In-situ formation of composite microstructures. *J. Microscopy*, 1985, **179**, 286–296.
24. van Hille, D., Bengtsson, S. and Warren, R., Quantitative metallographic study of fibre morphology in a short fibre reinforced aluminium alloy matrix. *Composites Science and Technology*, 1989, **35**, 195–206.
25. German, R. M., *Liquid Phase Sintering*. Plenum Press, New York, 1985, pp. 127–155.
26. Takajo, S., Kaysser, W. A. and Petzow, G., Analysis of particle growth by coalescence during liquid phase sintering. *Acta Met.*, 1984, **32**, 107–113.
27. Kaysser, W. A., Takajo, S. and Petzow, G., Particle growth by coalescence during liquid phase sintering of Fe–Cu. *Acta Met.*, 1984, **32**, 115–122.
28. Hwang, C. J. and Tien, T-Y., Microstructural development in silicon nitride ceramics. *Materials Science Forum*, 1989, **47**, 84–109.
29. Lai, K-R. and Tien, T-Y., Kinetics of β-Si_3N_4 in grain growth in Si_3N_4 ceramics sintered under high nitrogen pressure. *J. Am. Ceram. Soc.*, 1993, **76**(1), 91–96.
30. Lifzhitz, I. M. and Slyozov, V. V., The kinetics of precipitation from supersaturated solid solution. *J. Phys. Chem. Solid*, 1961, **19**(1/2), 35–50.
31. Wagner, C., Theorie der Alterung von Niederschlägen durch Umlösen. *Z. Elektrochem.*, 1961, **65**, 581–591.
32. Bowen, L. J., Weston, R. J., Carruthers, T. G. and Brook, R. J., Hot-pressing and the α-β transformation in silicon nitride. *J. Mater. Sci.*, 1978, **13**, 341–350.
33. O'Meara, C., Dunlop, G. L. and Pompe, R., Phase relationships in the system SiO_2–Y_2O_3–Al_2O_3. In *High Tech Ceramics*, ed. P Vincenzini. Elsevier Science Publishers, Amsterdam, 1987, pp. 265–270.
34. Campbell, G. H., Rühle, M., Dalgliesh, B. J. and Evans, A. G., Whisker toughening: A comparison between alumium oxide and silicon nitride toughened with silicon carbide. *J. Am. Ceram. Soc.*, 1990, **73**(3) 521–530.